New Benzo[*h*]quinolin-10-ol Derivatives as Co-sensitizers for DSSCs

Aneta Slodek [1], Paweł Gnida [2], Jan Grzegorz Małecki [1], Grażyna Szafraniec-Gorol [1], Pavel Chulkin [3], Marharyta Vasylieva [2], Jacek Nycz [1], Marcin Libera [1] and Ewa Schab-Balcerzak [1,2,*]

1 Institute of Chemistry, University of Silesia, 9 Szkolna Str., 40-006 Katowice, Poland; a.slodek@wp.pl or aneta.slodek@us.edu.pl (A.S.); jan.malecki@us.edu.pl (J.G.M.); grazyna.szafraniec-gorol@us.edu.pl (G.S.-G.); jacek.nycz@us.edu.pl (J.N.), marcin.libera@us.edu.pl (M.L.)
2 Centre of Polymer and Carbon Materials, Polish Academy of Sciences, 34 M. Curie-Skłodowska Str., 41-819 Zabrze, Poland; pgnida@cmpw-pan.edu.pl (P.G.); mvasylieva@cmpw-pan.edu.pl (M.V.)
3 Faculty of Chemistry, Silesian University of Technology, 9 Strzody Str., 44-100 Gliwice, Poland; pavel.chulkin@polsl.pl
* Correspondence: ewa.schab-balcerzak@us.edu.pl or eschab-balcerzak@cmpw-pan.edu.pl

Abstract: New benzo[*h*]quinolin-10-ol derivatives with one or two 2-cyanoacrylic acid units were synthesized with a good yield in a one-step condensation reaction. Chemical structure and purity were confirmed using NMR spectroscopy and elemental analysis, respectively. The investigation of their thermal, electrochemical and optical properties was carried out based on differential scanning calorimetry, cyclic voltammetry, electronic absorption and photoluminescence measurements. The analysis of the optical, electrochemical and properties was supported by density functional theory studies. The synthesized molecules were applied in dye-sensitized solar cells as sensitizers and co-sensitizers with commercial N719. The thickness and surface morphology of prepared photoanodes was studied using optical, scanning electron and atomic force microscopes. Due to the utilization of benzo[h]quinolin-10-ol derivatives as co-sensitizers, the better photovoltaic performance of fabricated devices compared to a reference cell based on a neat N719 was demonstrated. Additionally, the effect of co-adsorbent chemical structure (cholic acid, deoxycholic acid and chenodeoxycholic acid) on DSSC efficiency was explained based on the density functional theory.

Keywords: DSSC; 2-cyanoacrylic acid derivatives; co-adsorbents; EIS

1. Introduction

Much attention is currently being paid to renewable energy sources. This is related to increasing environmental pollution, the gradual depletion of fossil resources and environmental degradation. One of the most promising renewable energy sources is solar energy, which can be used for heating or converted into electricity [1]. It is worth paying particular attention to photovoltaics (PV), which have been widely and intensively developed in recent years [2–4]. In addition to well-known inorganic materials, organic materials are intensively tested in PV devices. Increased research on third generation PV cells accompanied the discovery and development of the first dye-sensitized solar cell (DSSC) in 1991 [5]. However, the DSSCs became more popular around the year 2000 when their efficiency exceeded 10% [6]. Additionally, they are gaining popularity and are constantly being researched due to their economic advantages: low cost of fabrication, high power conversion efficiency, and relatively straightforward procedures of manufacturing [5,7]. It is worth noting that the DSSC cell consists of several key elements, including the dye used. The dye is responsible for absorbing incident photons and injecting electrons into the TiO_2 conduction band [8]. Currently, metal-containing complexes such as N3, N719, N749 based on Ru or YD2 with Zn are mainly utilized to prepare dye-sensitized solar cells [9–12]. However, metal-containing dyes are expensive to obtain and the purification

process is very complicated and tedious [13–16]. Therefore, research is being carried out to reduce the use of sensitizers containing metal atoms by looking for new metal-free dyes that are cheaper and easier to synthesize. Organic sensitizers are used in exchange for metal-dyes or as a co-sensitizer to reduce the amount of commercial dyes used. Very important at the design level are the properties that the new dye should exhibit, including good solubility in solvents, wide absorption range of sunlight, high molar coefficient, resistance to photodegradation and photocorrosion, thermal and electrochemical stability, and appropriate alignment of the frontier molecular orbital energy levels [17–22]. It was found that co-sensitization using two or more sensitizers is an effective approach to achieve highlight harvesting efficiency [23,24]. Two groups of DSSC can be specified. The first one is based on two dyes, one of which is a new metal-free dye, and the other is a commercial metal-containing sensitizer, which is often Ru (e.g., N719, N3, HD-2) [7,23–32]. It is worth noting that these PV cells exhibit higher efficiencies than devices containing only commercial dye in most cases. Even if the efficiencies are comparable or slightly lower than those of the reference DSSC, a correspondingly less amount of metal-dye amount is used, which reduces the cost of preparing the solar cell [33–35]. The second group constitutes DSSC, sensitized only, with new metal-free dyes [33,35–41].

Herein, two new benzo[*h*]quinolin-10-ol cyanoacrylic acid derivatives are presented for use as co-sensitizers with commercial N719 dye in DSSC devices. The properties of new compounds based on thermal, UV-vis, photoluminescence, and cyclic voltammetry measurements are determined. Additionally, functional density theory (DFT) estimates the frontier molecular orbitals of the synthesized molecules, UV-vis spectra adsorbed on TiO_2, and binding energies of the dyes on TiO_2 applied. Moreover, the impact of the chemical structure of typically used adsorbents, such as chenodeoxycholic acid (CDCA), cholic acid (CA), and deoxycholic acid (DCA) on device performance based on N719 was explained by DFT. The fabricated devices were characterized by the current density-voltage (J-V) curves and electrochemical impedance spectroscopy (EIS). It was demonstrated that the new simple molecules, applied as co-sensitizer with N719, allowed us to obtain higher or comparable efficiencies to reference cells based only on expensive N719 dye.

2. Experimental

All chemicals were commercially available and were used without further purification. 10-Hydroxybenzo[*h*]quinoline-9-carboxaldehyde and 10-hydroxybenzo[*h*]quinoline-7,9-dicarboxaldehyde were synthesized, as has been reported [42]. The chemicals, instrumental equipment applied for synthesized compounds and solar cells characterization and DSSC preparations are presented in Supplementary Material.

2.1. Computational Details

All theoretical calculations were performed using Gaussian 16, Revision C.01, program package [43] at DFT or TD-DFT level. The singlet state geometry optimizations, frequency and electronic transition calculations were made with the use of B3LYP functional [44,45] with the 6-31G(d,p) basis set [46]. Calculations were made in the gas phase except for the absorption electronic spectra of 1a, 2a compounds (Figure S3) in addition to the PCM model [47], with DMF as a solvent. The density of states diagrams (Figure S13) was obtained with GaussSum [48]. The adsorption energies (E_{ads}) of the dyes were evaluated using the following expression, $E_{ads} = E_{dye} + E_{TiO2} - E_{dye}@TiO_2$, where E_{dye}, E_{TiO2} and $E_{dye}@TiO_2$ are the energies of dye, TiO_2, and total system (dye@TiO_2). The Gibbs free energies of the dye@TiO_2 species were calculated at 298.15 K.

2.2. Synthesis of Cyanoacrylic Acids 10-Hydroxobenzo[h]Quinoline Derivatives

Carboxaldehyde and cyanoacetic acid (6 eq. for compound **1**; 16 eq. for compound **2**) were loaded into a Schlenk flask equipped with a magnetic stir bar. The flask was evacuated and flushed with argon for three cycles. Next, a mixture of MeCN/CHCl₃ (3:1) was added, and the mixture was again evacuated and flushed with argon. Then, piperidine (12 eq. for

compound **1**; 22 eq. for compound **2**) was added, and finally, the flask was flushed with argon and evacuated. The mixture was heated at 90 °C for 24 h. After being cooled to room temperature, the mixture was evaporated under reduced pressure, water was added, and the crude product was extracted with CH_2Cl_2. The organic layer was collected and dried over anhydrous $MgSO_4$. After filtration, the solvent was removed under reduced pressure. The residue was purified by crystallization from a mixture of $EtOH/Et_2O$.

10-Hydroxybenzo[*h*]quinoline-9-cyanoacrylic acid (**1a**) Yield: 54%. ^{1}H NMR (400 MHz, DMSO) δ 9.04 (d, *J* = 4.4 Hz, 1H), 8.66 (m, 1H), 8.61 (d, *J* = 8.0 Hz, 1H), 8.19 (d, *J* = 8.4 Hz, 1H), 8.10–8.03 (d, *J* = 8.4 Hz, 1H), 7.99–7.92 (m, 1H), 7.83 (m, 2H). ^{13}C NMR (101 MHz, DMSO) δ 165.20, 162.17, 146.40, 142.74, 138.59, 134.00, 128.97, 128.16, 126.29, 125.44, 122.28, 120.56, 119.88, 118.66, 117.85, 114.99, 114.88, 111.13. Elem. Anal. (%) Calcd for $C_{17}H_{10}N_2O_3$: C, 70.34; H, 3.47; N, 9.65. Found: C, 70.18; H, 3.77; N, 9.84.

10-Hydroxybenzo[*h*]quinoline-7,9-di(cyanoacrylic) acid (**2a**): Yield: 60%. ^{1}H NMR (400 MHz, DMSO) δ 9.12 (d, *J* = 4.4 Hz, 1H), 8.91 (s, 1H), 8.76 (d, *J* = 8.0 Hz, 1H), 8.60 (d, *J* = 1.8 Hz, 2H), 8.17 (d, *J* = 8.8 Hz, 1H), 8.07 (d, *J* = 8.8 Hz, 1H), 7.94–7.91 (m, 1H). ^{13}C NMR (101 MHz, DMSO) δ 165.01, 164.63, 162.14, 146.86, 146.68, 142.74, 138.56, 134.80, 128.97, 128.18, 126.29, 124.22, 123.17, 120.52, 119.17, 118.65, 117.49, 114.99, 114.94, 114.86, 111.42. Elem. Anal. (%) Calcd for $C_{21}H_{11}N_3O_3$: C, 65.46; H, 2.877; N, 10.905. Found: C, 65.06; H, 2.93; N, 10.41.

3. Results and Discussion

3.1. Synthesis, Thermal, Optical and Electrochemical Characterization

The preparation route and chemical structure of novel compounds 10-hydroxybenzo[*h*]quinoline-9-cyanoacrylic acid and 10-hydroxybenzo[*h*]quinoline-7,9-di(cyanoacrylic) acid, denoted as **1a** and **2a**, respectively, are presented in Figure 1. The synthesis of the cyanoacrylic acids 10-hydroxobenzo[*h*]quinoline derivatives (**1a** and **2a**) was carried out by the Knoevenagel condensation reaction of **1** and **2** in the presence of cyanoacetic acid and piperidine. The aldehyde precursors **1** and **2** were prepared according to the previously described procedure [42].
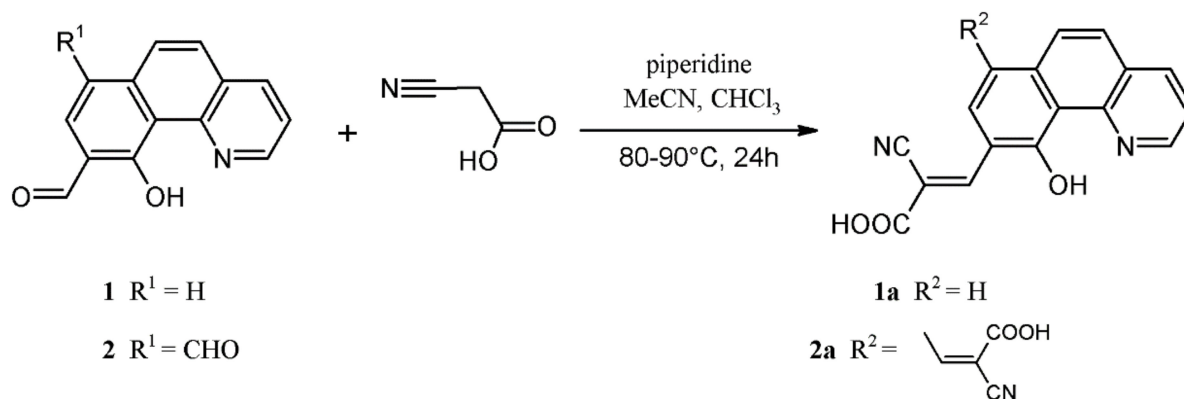

Figure 1. Synthetic route for the preparation of benzo[*h*]quinolin-10-ol derivatives **1a** and **2a**.

The desired dyes **1a** and **2a** were obtained in good yield (54–60%) as an orange (**1a**) and red solid (**2a**). The ^{1}H and ^{13}C NMR spectroscopic characterization and elemental analysis confirmed its chemical structure and purity. DSC thermograms registered in the first heating scan showed the melting endotherms with a maximum at 240 and 175 °C, for **1a** and **2a**, respectively (cf. Figure S1). The second heating run, recorded after cooling, revealed only the glass transition (T_g) temperature at 202 (**1a**) and 119 °C (**2a**), and during further heating, no additional peaks were seen. It shows that the prepared compounds are molecular glasses, which form a stable glassy phase. The presence of a second cyanoacrylic acid group lowered the melting point, but conversely, slightly impacted T_g.

The electronic absorption and photoluminescence (PL) spectra of the cyanoacrylic acids 10-hydroxobenzo[*h*] quinoline derivatives in methanol (MeOH) and dimethylformamide (DMF) are shown in Figure 2, and the data are listed in Table 1. Additionally, the UV-vis data of starting aldehydes (**1** and **2**) are given in Figure S2 and Table S1.
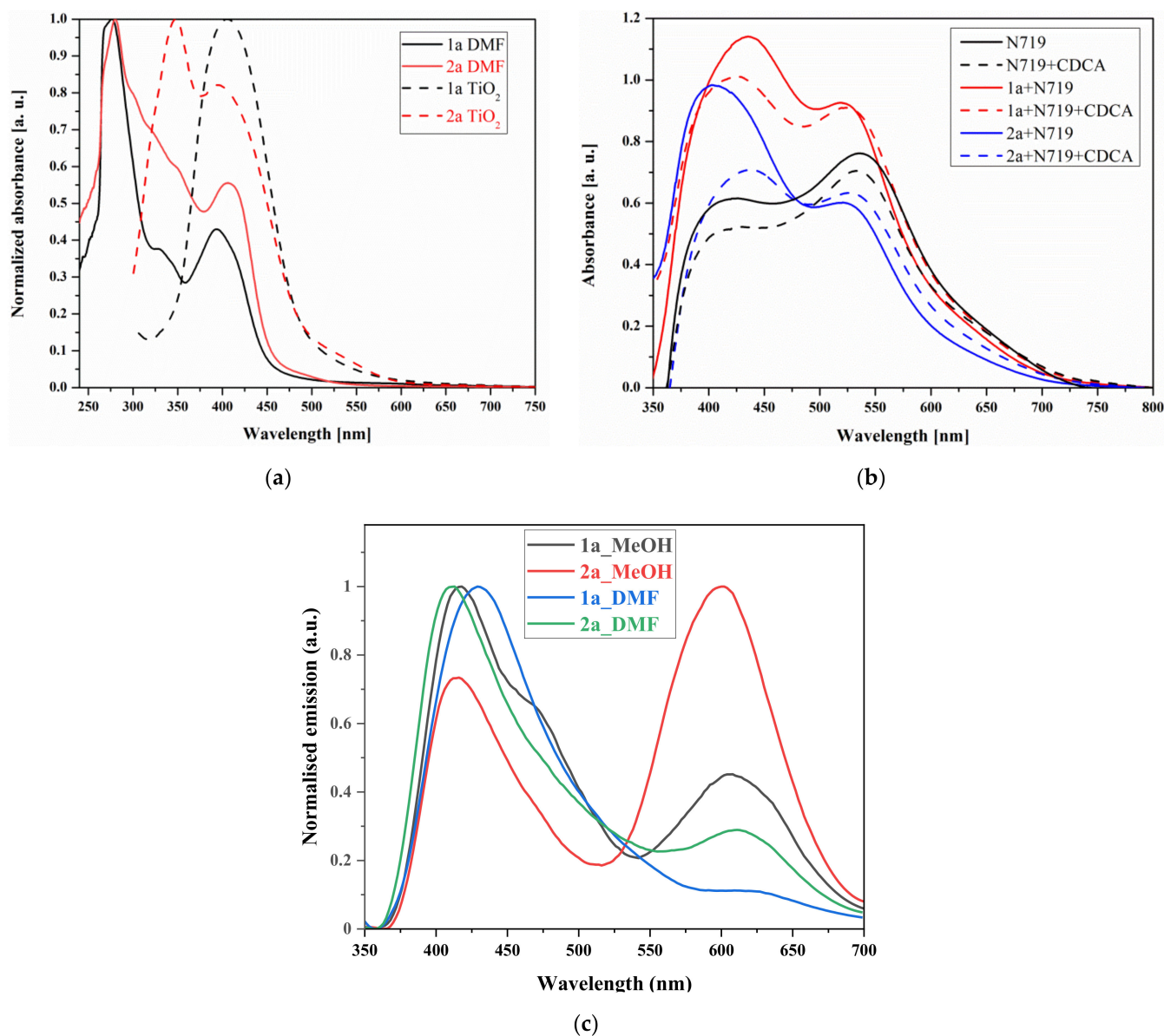
(a)

(b)

(c)

Figure 2. (**a**) UV-vis spectra of **1a** and **2a** in solution and TiO$_2$ films with adsorbed dyes on glass substrates, (**b**) **1a** and **2a** as co-sensitizers with N719 with or without CDCA addition and (**c**) photoluminescence spectra of **1a** and **2a** recorded in the MeOH and DMF solutions (c = 10^{-5} mol/L).

Table 1. Photophysical data for **1a** and **2a** recorded in MeOH and DMF solutions.

Solvent	λ_{max} (nm) (ε (M^{-1}cm^{-1}))		PL λ_{em} (nm)		τ_{eff} (τ (ns) (Weight%))		Φ (%)		E_g^{OPT} (eV)	
	1a	**2a**	**1a**	**2a**	**1a**	**2a**	**1a**	**2a**	**1a**	**2a**
MeOH	275(10,880), 327(4635), 393(5085)	273(23,896), 366(13,600), 383 (12,727)	418, 611	413, 601	5.56 [1.65 (21.24), 6.62(78.76)]	5.97 [1.71(12.94), 6.60(87.06)]	0.07	0.15	2.97, 2.03	3.00, 2.06
DMF	276(16,000), 328(6000), 391(6667)	289(10,000), 354(10,667), 407(10,000)	430, 626	411, 610	4.24 [1.19(39.9), 6.26(60.1)]	4.57 [1.17(45.04), 7.35(54.96)]	1.13	1.25	2.89	3.02, 2.03

The synthesized compounds (**1a** and **2a**) reveal two absorption bands, with one of them assigned to the π-π* electronic excitations localized within the conjugated system, ranging from 260 to 360 nm, and with a maximum of 278 (**1a**), 280 (**2a**) nm and shoulder of 328 (**1a**), 354 nm (**2a**), respectively. The second is seen at a lower energy range with λ_{max} at 391 (**1a**) and 407 (**2a**), which can be attributed to the intramolecular charge transfer (ICT) from 10-hydroxybenzo[*h*]quinoline to the electron withdrawing anchoring fragment. The λ_{max} of ICT of **2a** is bathochromically shifted (16 nm), and the band is broader and in a visible range compared to **1a**. Usually, the increase in cyanoacrylic acid groups shifts the absorption range to a lower energy [23,25]. In this case, the effect of the number of cyanoacrylic acid units on the electronic absorption range is weakly pronounced. A good match between the experimental and obtained from DFT calculations absorption spectra was observed (cf. Figure 3). Compound **2a**, with two anchoring groups, exhibits a higher molar absorption coefficient (ε = 10,667 at 354 nm and 10,000 $M^{-1}cm^{-1}$ at 407 nm) than compound **1a** with one cyanoacrylic acid moiety (ε = 6000 at 328 nm and 6667 $M^{-1}cm^{-1}$ at 391 nm) in DMF. Thus, a higher molar absorption coefficient and red-shifted spectrum of **2a** can be advantageous for a higher DSSC efficiency.
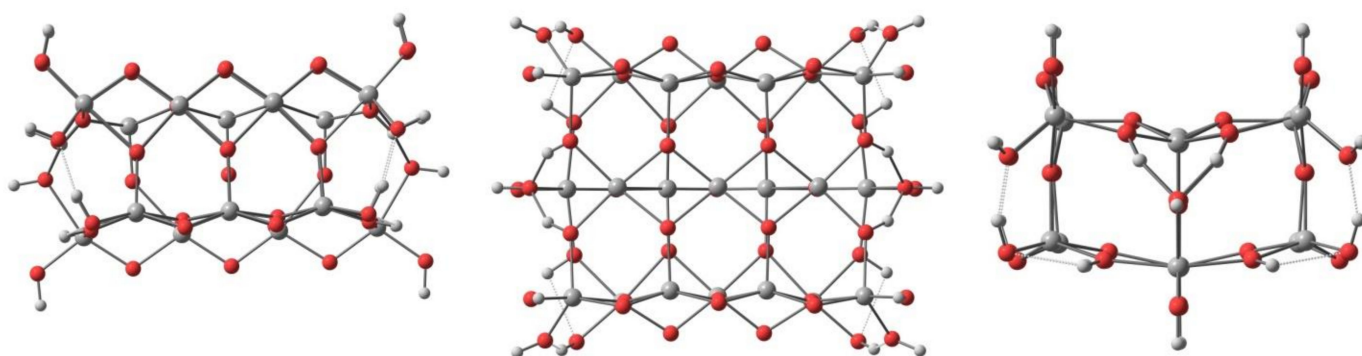

Figure 3. The top, front and side view of the $Ti_{21}O_{54}H_{24}$ cluster.

When comparing the UV-vis spectra of **1a** and **2a** with the absorption of aldehydes, it was found that the replacement of CHO units in **1** and **2** by the cyanoacrylic acid group in **1a** and **2a** results in a bathochromic shift of 10 nm in the ICT peak in the case of **1a**, while for **2a**, the position of ICT remains unchanged (Table 1 and Table S1). The absorption shapes of **1** and **1a** are similar, whereas in the case of **2a**, the $S_0 \rightarrow S_2$ transition is weakly expressed when compared to compound **2**. Conversely, compounds **1a** (ε_{max} = 5085 $M^{-1}cm^{-1}$) and **2a** (ε_{max} = 12,727 $M^{-1}cm^{-1}$) have a considerably higher molar extinction coefficient for the $S_0 \rightarrow S_1$ transition compared to both aldehyde derivatives **1** (ε_{max} = 4505 $M^{-1}cm^{-1}$) and **2** (ε_{max} = 208 $M^{-1}cm^{-1}$) in methanol solution.

Next, the absorption nature of synthesized compounds adsorbed into TiO_2 was tested. Figure 2a displays the UV-vis spectra of a **1a** and **2a** measured for TiO_2 films with adsorbed dyes. In the UV-vis spectra of **1a** and TiO_2 system (**1a**@TiO_2) one band with a maximum at 406 nm was observed. In the case of **2a**@TiO_2 band, two structured maxima at 350 and 395 nm is seen. When the solution state and TiO_2 systems spectra were compared, both adsorbed molecules shown shifted absorption, which is likely due to aggregation [49,50]. Moreover, TiO_2 with dyes exhibited an extended absorption curve up to 600 nm, which was about 150 nm higher than the solution state absorption curve, probably due to the J-aggregates' formation [49,50]. Considering the UV-vis spectra of TiO_2 with dyes, the broader absorption covering the range from 300 to 600 nm exhibited **2a**@TiO_2 compare to **1a**@TiO_2 which absorbed radiation from 340 to 600 nm (cf. Figure 2). The effect of chenodeoxycholic acid (CDCA) as co-adsorbent on UV-vis properties of the prepared photoanodes was also studied. Some of the most commonly used co-adsorbents for DSSC are cholic acid (CA), deoxycholic acid (DCA) and chenodeoxycholic acid (CDCA). In this article, CDCA was selected based on our previous results [51], and the DFT calculations described herein in Section 3.2.1. The expected decrease in absorbance of the photoanode

containing CDCA was seen (cf. Figure 2b). The working principle of the co-adsorbent is based on the adsorption of CDCA particles instead of dye molecules, which reduces the formation of dyes aggregates. Due to the smaller number of dye molecules anchored to the TiO$_2$ surface, the absorbance decreases.

In PL spectra of **1a** and **2a**, two emission maxima in the range of 400–675 nm are seen. Similar to absorption spectra, a hypsochromic shift in emission spectra was observed for bi anchoring **2a** compared to mono anchoring **1a**. Compounds **1a** and **2a** demonstrate very weak fluorescence in both solutions with the PL quantum yields range from 0.07 to 1.25% higher for bi anchoring dye **2a** (Table 1). A comparable increase in quantum efficiency was observed for the pyrazolo[3,4-*b*]quinoline and phenothiazine derivatives when increasing the number and/or strength of electron withdrawing substituents [52,53]. Compounds **1a** and **2a** possess bixponential fluorescence decay in both solvents (Table 1 and Figure S4). The efficient lifetimes of **1a** and **2a** are comparable in the same solvent and slightly shorter in DMF (4.24–4.57 ns) than in MeOH (5.56–5.97 ns). The time-resolved data and emission range imply that for dyes **1a** and **2a**, the ICT character is lessened, and the fluorescence may originate from $\pi \rightarrow \pi^*$ excited state because ICT is a competitive relaxation process of the singlet excited state and typically reduces the fluorescence [54].

The cyclic voltammetry (CV) measurements were carried out to study the electrochemical behavior of the synthesized benzo[*h*]quinolin-10-ol derivatives and N719 in Bu$_4$NPF$_6$/DMF solution. During the CV experiment, the reduction process was not observed, and oxidation processes for **2a** and N719 were seen (Figure S4). The oxidation potential onset (E$_{ox}^{onset}$) of **2a** was higher (0.53 V) compared to N719 (0.33 V). A slightly higher oxidation potential (0.35 V) of N719 was determined from DPV measurements (Figure S5). Comparing the structure of **2a** and **1a**, it is expected that the oxidation potential of **2a** (with two electron withdrawing groups) should be lower than **1a** [54]. It can be assumed that the oxidation potential of **1a** is higher than 0.53 V (**2a**). Unfortunately, it is impossible to measure the higher potential in DMF. Changing the solvent was not considered, due to the limited solubility of these compounds. Based on the oxidation onset, the potential HOMO energy level was calculated assuming that the IP of ferrocene equals −5.1 eV [55], being −5.73 and −5.63 eV for **2a** and N719, respectively. HOMO levels are somewhat more negative than the I$^-$/I^{3-} redox potential (−4.8 eV) [32], and should enable the dye regeneration. The LUMO energy level determined from the optical energy gap (Eg^{OPT}), and calculated HOMO to be −3.03 and −3.47 eV for 2a and N719, respectively. A HOMO energy level of N719 was reported in the literature from UPS (−5.34 eV vs vacuum) and CV in DMF (−5.37 eV vs vacuum); these measurements are similar to our experimental result [56,57]. However, the lower HOMO energy level in the range of 6.0–6.14 eV obtained in different CV experimental conditions was also reported [58–60]. Additionally, CV measurements of N179 were carried out in acetonitrile (ACN) and DMF with various scanning rates. In both cases, an irreversible oxidation process was demonstrated (Figure S6, Table S2). At different scan rates, the beginning of the peak did not change.

3.2. Computational Studies

Density functional theory (DFT) studies were applied for (i) explanation of the co-adsorbents chemical structure importance, (ii) both neat compounds and dye-TiO$_2$ system geometry optimizations and frontier molecular orbitals energy determination of **1a** and **2a,** and (iii) UV-vis absorption spectra calculations of dyes in solution and dye-TiO$_2$ systems.

3.2.1. Importance of Co-Adsorbents Chemical Structure

The co-adsorbents are applied for DSSC photoanode preparation to limit the dye aggregates formation onto TiO$_2$ surface which may improve the photovoltaic performance of the device. As co-adsorbents, chenodeoxycholic acid (CDCA), cholic acid (CA) and deoxycholic acid (DCA) are usually used [61]. Among them, the beneficial impact of CDCA on DSSC efficiency was presented in our previous work [51]. Moreover, based on DFT, G. Saranya et al. [62] showed that CDCA co-adsorbent is a crucial component of a

high-performance DSSC; they studied effect of CDCA on the properties of the dye denoted as TY6′ and TiO$_2$ interface. It was found that CDCA not only stabilizes the TY6′/TiO$_2$ system, but also prevents the surface tensile stress induced by the dye monolayer [62].

Considering the chemical structure of CDCA, CA, and DCA, they differ structurally only by their R substituents. There is a lack of an explanation of the effect of the chemical structure of CA, DCA, and CDCA on DSSC performance in the literature. Thus, to explain the impact of co-adsorbents CDCA, CA and DCA chemical structure, DFT was used. The geometric optimizations and frequency calculations were made with the use of functional B3LYP [44,45] with the smaller 6-31G(d) basis set [46]. The calculations were carried out with the Gaussian 16, Revision C.01 program [43]. The molecular geometry, HOMO and LUMO contours of the Ti$_{21}$O$_{54}$H$_{24}$ cluster, CA, CDCA, DCA co-adsorbent, as well as the adsorbed *enol*–forms of the compounds on Ti$_{21}$O$_{54}$H$_{24}$ cluster are given in Table S3.

A TiO$_2$ surface model was built by cutting two trilayers from the bulk experimental geometry (with Ti–O bond lengths of 1.948 Å and 1.981 Å) and closed by hydrogen atoms (with optimized positions) forming terminal hydroxyl groups, which led to a Ti$_{21}$O$_{54}$H$_{24}$ cluster (Figure 3).

A two-trilayer thickness was used to allow fivefold coordinated Ti atoms on the surface. Toward the other two directions, the model's size was chosen to have a central fivefold coordinated Ti atom on the surface with two neighbouring fivefold coordinated Ti atoms and two neighbouring bridging oxygen atoms.

Two types, monodentate through C=O and bidentate bridging, namely the *enol*– and *keto*– forms, of anchoring modes of the dyes were calculated. The Ti–O$_{carboxylate}$ bond distances in *enol*–form (cf. Table S4) of 2.23 Å (CA), and 2.18 Å (CDCA, DCA) are longer than in the case of *keto*—bidentate form, where the distances are 2.11, 2.14 Å in CA, 2.09, 2.14 in CDCA and 2.09 and 2.18 Å in DCA. Thus, the bidentate bridging mode creates a more stable system. This is especially evident in the case of CA dye, for which the calculated adsorption energy of *keto*–form is 12 kcal/mol higher compared to the *enol*– one. The adsorption energies, calculated using the expression $E_{ads} = E_{dye} + E_{TiO2} - E_{dye@TiO2}$, where E_{dye}, E_{TiO2} and $E_{dye@TiO2}$ are the energies of dye, Ti$_{21}$O$_{54}$H$_{24}$, and total system (dye@ Ti$_{21}$O$_{54}$H$_{24}$) of the *enol*– forms of these dyes are similar to the differences, do not exceed 2.4 kcal/mol (cf. Figure 4 and Table S4).

The *keto*–form of CA shows a higher adsorption energy by about 9 kcal/mol than CDCA and DCA dyes. Moreover, one of the hydroxyl groups of CA molecule forms a hydrogen bond with TiO$_2$, which results in the slope of the carbon skeleton and prevents interaction of sensitizer and TiO$_2$ surface (Figure 5).

The adsorbed CDCA molecule is almost perpendicular to the TiO$_2$ surface. The slope of the carbon skeleton increases with CDA and reaches a significant value for CA (cf. Figure S7). Thus, the high adsorption energy, highest G_{ads} and the bent geometry of the carbon skeleton of the adsorbed CA molecule indicate the smallest suitability for use in cells among the dyes tested. The adsorption energies of CDCA and DCA molecules are similar, however, taking into account the almost perpendicular adsorption of the CDCA molecule and the slightly higher value of G_{ads}, it can be assumed that CDCA is a better co-adsorbent than DCA.
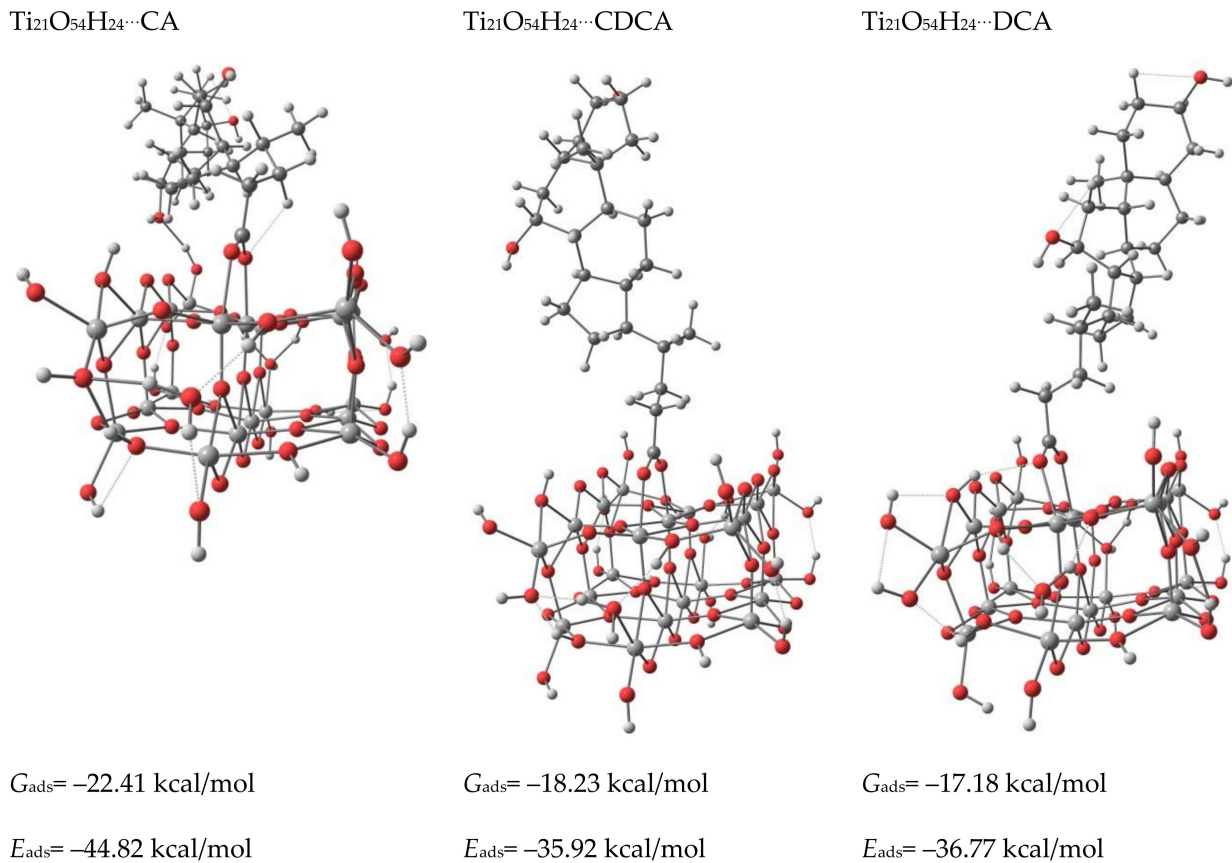
$Ti_{21}O_{54}H_{24}\cdots CA$

$Ti_{21}O_{54}H_{24}\cdots CDCA$

$Ti_{21}O_{54}H_{24}\cdots DCA$

G_{ads}= −22.41 kcal/mol

E_{ads}= −44.82 kcal/mol

G_{ads}= −18.23 kcal/mol

E_{ads}= −35.92 kcal/mol

G_{ads}= −17.18 kcal/mol

E_{ads}= −36.77 kcal/mol

Figure 4. Adsorbed *keto*- forms of the dyes on $Ti_{21}O_{54}H_{24}$ cluster (The Gibbs free energies G of the Scheme 298.15 K).
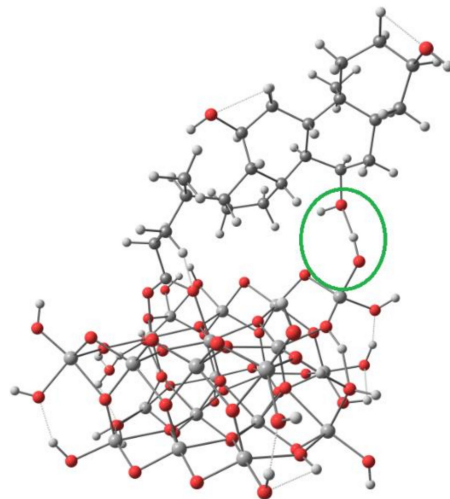

Figure 5. Hydrogen bond in the $Ti_{21}O_{54}H_{24}\cdots CA$ system.

3.2.2. Dye and Dye-TiO$_2$ System Geometry Optimizations and Frontier Molecular Orbitals Energy Determination

The geometry optimizations and frequency calculations were made with of the use the B3LYP functional [44,45] with the 6-31G(d,p) basis set [63,64]. The calculations were carried out with the Gaussian 16, Revision C.01 program [43]. Adsorbed **1a** and **2a** molecules on the clusters are presented in Figure 6.
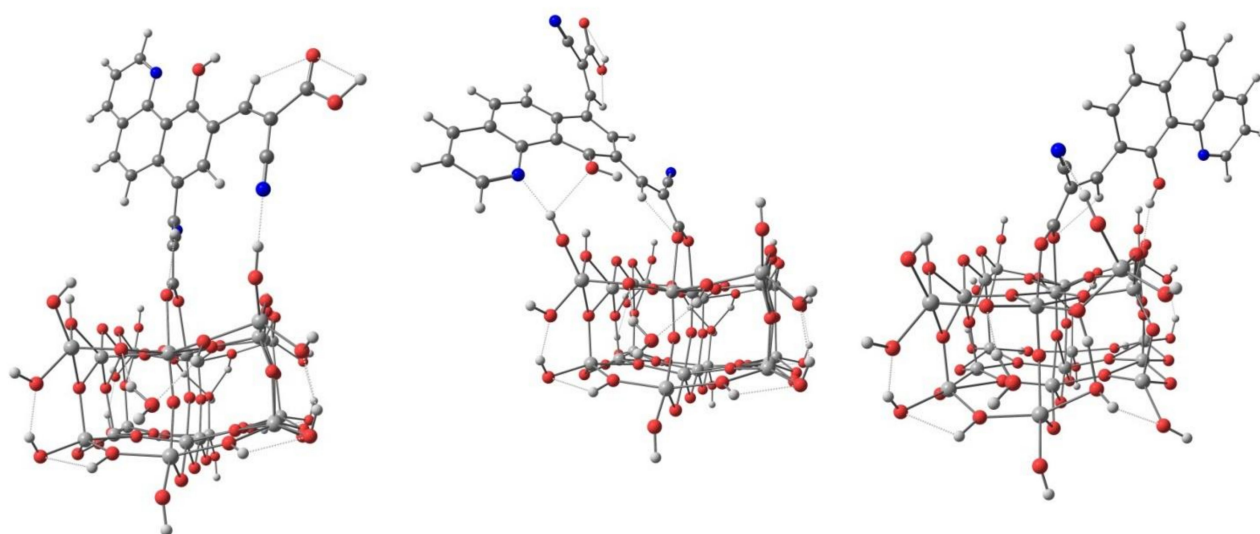
Ti$_{21}$O$_{54}$H$_{24}$···**2a-a**

ΔG_{ads} = −115.93 kcal/mol

E_{ads} = −42.11 kcal/mol

Ti$_{21}$O$_{54}$H$_{24}$···**2a-b**

ΔG_{ads} = −18.66 kcal/mol

E_{ads} = −37.37 kcal/mol

Ti$_{21}$O$_{54}$H$_{24}$···**1a**

$\Delta G_{ad\,s}$ = −34.82 kcal/mol

E_{ads} = −52.72 kcal/mol

Figure 6. Adsorption of **1a** and **2a** on Ti$_{21}$O$_{54}$H$_{24}$ clusters (Gibbs free energies G of the species were calculated at 298.15 K).

To obtain the binding energies of the dyes on TiO$_2$, the structures of **1a**, **2a** and Ti$_{21}$O$_{54}$H$_{24}$ cluster were optimized separately (cf. Section 3.2.1), before the dye@Ti$_{21}$O$_{54}$H$_{24}$ systems were optimized. During the optimization of the dye@Ti$_{21}$O$_{54}$H$_{24}$ system, the carboxylic proton of the dye was transferred to a nearby oxygen atom of the TiO$_2$. Hence, the dyes were adsorbed on TiO$_2$ with a bidentate bridging mode. Due to the intimate contact between carboxylate anchor-based dyes and the metal oxide surface, the structures with bidentate bridging modes exhibit superior stability compared to other types of anchoring modes. Because of the presence of two carboxyl groups in the **2a** molecule, the geometries of two possible types (**2a-a** and **2a-b**) of adsorption of this compound on the TiO$_2$ surface have been optimized. Adsorption energies calculated using the expression $E_{ads} = E_{dye@TiO2} − (E_{dye} + E_{TiO2})$, where E_{dye}, E_{TiO2} and $E_{dye@TiO2}$ are the energies of dye, Ti$_{21}$O$_{54}$H$_{24}$, and total system (dye@Ti$_{21}$O$_{54}$H$_{24}$). The obtained binding energies were −42.11, −37.37 and −52,72 kcal/mol for **2a-a**, **2a-b** and **1a**, respectively. The Ti–O$_{carboxylate}$ bond distances are of 2.16, 2.18 Å in **2a-a**@Ti$_{21}$O$_{54}$H$_{24}$, 2.14, 2.21 Å in **2a-b**@Ti$_{21}$O$_{54}$H$_{24}$ and in the case of **1a**@Ti$_{21}$O$_{54}$H$_{24}$ the distances are 2.11 and 2.18 Å. The higher adsorption energy, and especially the high value of ΔG_{ads}, indicates that the interaction of **2a** with TiO$_2$ takes place through the carboxylate group in position 7 of the benzoquinoline ring i.e., in the form presented in Figure 6 as Ti$_{21}$O$_{54}$H$_{24}$··· **2a-a**. Adsorption through the carbonyl group in the *trans* position to the hydroxyl group in the benzoquinoline ring is also strengthened by the direction of the molecule's dipole moment, as shown in Figure S8 in the Supplementary Materials.

In the case of both dyes, there is a possibility of the formation of hydrogen bonds between the dye molecule and the TiO$_2$ surface (cf. Figure S9). Whereas in the **2a-a**@Ti$_{21}$O$_{54}$H$_{24}$ system, a cyano group and a proton belonging to the hydrated TiO$_2$ surface are involved in such a bond, of **2a-b**@Ti$_{21}$O$_{54}$H$_{24}$ the hydroxyl group on the surface interacts with the nitrogen atom in the benzoquinoline ring. Two types of hydrogen bonds are possible in the **1a**@Ti$_{21}$O$_{54}$H$_{24}$ system. One between the –C≡N group and hydrated titanium oxide, and the second between the hydroxyl group at position 10 of the benzoquinoline ring and the oxygen of TiO$_2$.

The geometry of the adsorbed molecules in the range of angles between the plane of the benzoquinoline ring and the carboxylate anchor group is significantly different

from that of free dye molecules (cf. Figures S10 and S11, and Table S5). In adsorbed dye molecules, the plane of aromatic rings is twisted in relation to the plane of the 2-cyanoacrylic unit, and additionally in the **2a-b**@$Ti_{21}O_{54}H_{24}$ and **1a**@$Ti_{21}O_{54}H_{24}$ the benzoquinoline rings, which are tilted over the TiO_2 surface. The relatively smallest changes occur in the thermodynamically and energetically privileged **2a-a**@$Ti_{21}O_{54}H_{24}$ system, for which the angle between the benzoquinoline plane and the titanium dioxide surface does not differ much from the right angle (85.17°). Moreover, the internal geometry of the **2a** molecule adsorbed by carboxylate anchor in position 7 of benzoquinoline changes slightly, while the plane of the aromatic rings is twisted in relation to the plane of the carboxylate group only by about 5°.

The frontier molecular orbitals (FMO) of the dyes adsorbed on $Ti_{21}O_{54}H_{24}$ system (c.f. Figure S12) reveal that HOMOs are localized in the dye while LUMOs have the shape of the lobes characteristic of *d*-type orbitals of titanium atoms. The analysis of the density of states diagrams (cf. Figure S13) shows that in **2a**@$Ti_{21}O_{54}H_{24}$, the dye orbitals have a certain share (14%) of the HOMO level. In the case of the **1a**@$Ti_{21}O_{54}H_{24}$ system, HOMO is located entirely on the dye (99%). Thus, the contribution of the dye is more significant in the valence band. LUMO in both systems is located on the $Ti_{21}O_{54}H_{24}$.

The UV-vis spectra of the **2a**@$Ti_{21}O_{54}H_{24}$ and **1a**@$Ti_{21}O_{54}H_{24}$ were simulated in a vacuum using TF-DFT formalism depicted in Figure 7.
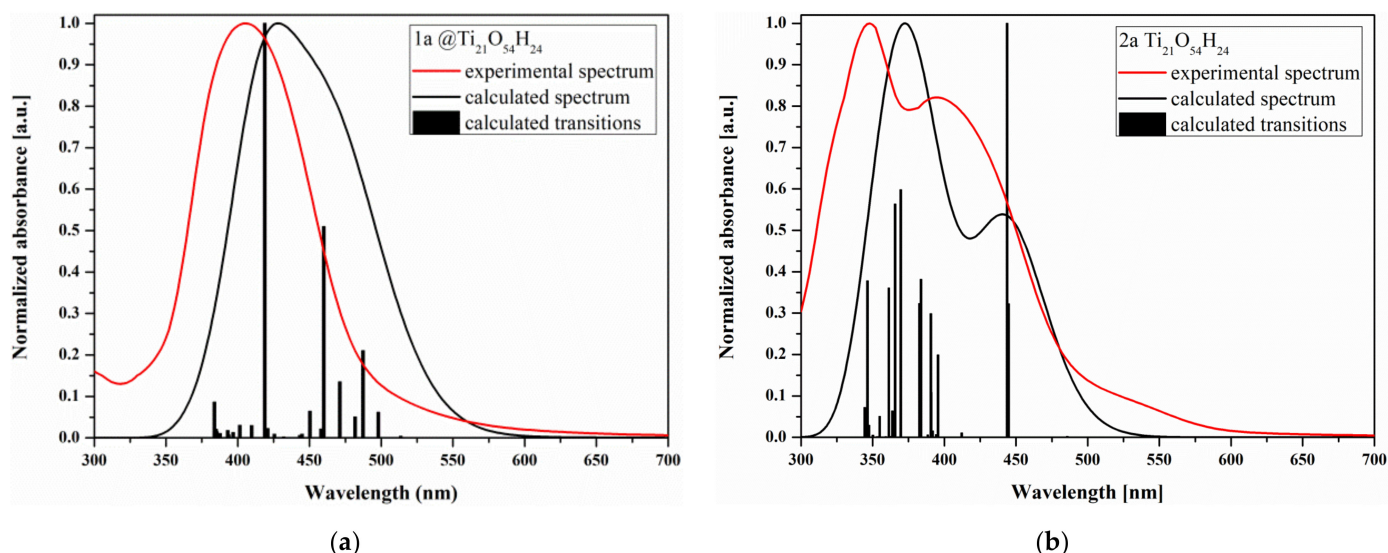
Figure 7. Normalized calculated and experimental UV-vis spectra of (**a**) **1a** or (**b**) **2a**@$Ti_{21}O_{54}H_{24}$ systems.

The transitions calculated in the visible range of the electronic absorption spectrum correspond to the excitations between the HOMO and the lowest energetically LUMO levels. Considering the location of the HOMO and LUMO orbitals (cf. Table S6), it can be concluded that in the case of **1a**, the process of charge transfer from the dye molecule to TiO_2 is more pronounced. This is due to the fact that the HOMO orbital in the **1a**@$Ti_{21}O_{54}H_{24}$ system is located on the dye molecule, while in **2a**@$Ti_{21}O_{54}H_{24}$ the proportion of the dye in HOMO is 14%. Thus, considering the calculation results concern FMO appear that **1a** could be a better sensitizer than **2a**, however, a wider range of absorption, the thermodynamics of adsorption as well as changes in the geometry of the adsorbed dyes indicate **2a-a** as a better sensitizer.

3.3. DSSCs Characterization

The synthesized cyanoacrylic acids 10-hydroxobenzo[*h*]quinoline derivatives (**1a** and **2a**) were applied as sensitizers and co-sensitizers in DSSCs. Photovoltaic devices with a FTO/TiO_2 + dye/EL-HSE/Pt/FTO structure were fabricated. The three types of PV cells were prepared: (i) with a neat **1a** and **2a**, (ii) with a mixture of a new dye with the N719

and (iii) with a mixture of dyes and co-adsorbent. As co-adsorbent, based on our previous studies (described in [51]), and the DFT results presented in Section 3.2.1, chenodeoxycholic acid (CDCA) was selected. Moreover, the reference cell with N719 was constructed.

3.3.1. Photoanode Thickness and Morphology

In the first step of the investigation, prepared photoanodes' thickness and surface morphology were investigated using optical, scanning electron (SEM) and atomic force microscopes (AFM). The TiO$_2$ layer thickness significantly impacts the photovoltaic parameters of the solar cells. The thicker layers can adsorb more dye molecules, but too much absorbed molecules may cause higher electron transport resistance and increase the recombination of electron with I$_3^-$ on the TiO$_2$ surface, which decrease the open-circuit voltage (V$_{oc}$) of the device and, consequently, lower the power conversion efficiency (PCE). Additionally, too thick an oxide layer may limit electron generation. Conversely, in thin TiO$_2$ layers, not enough dye number can be anchored, causing a decrease in short-circuit current (J$_{sc}$) values, which is reflected in PCE reduction [51,65,66]. The obtained TiO$_2$ layers with adsorbed dyes molecules thickness, root-mean-square (RMS) determined based on AFM and root-mean-square roughness (S$_q$) and sharpness of the roughness profile (S$_{ku}$) obtained from optical microscope measurements are collected in Table 2.

Table 2. Characterization of the prepared photoanodes based on SEM, AFM and optical microscope measurements.

Photoanode	AFM	SEM	Optical Microscope		
	RMS (nm)	Thickness (µm)	Thickness (µm)	S$_q$ (µm)	S$_{ku}$
TiO$_2$ + 1a	32	9	8	0.459	4.159
TiO$_2$ + 2a	33	10	10	0.319	4.707
TiO$_2$ + 1a + N719	29	8	9	0.383	4.331
TiO$_2$ + 2a + N719	31	11	10	0.311	4.924
TiO$_2$ + 1a + N719 + CDCA	35	12	12	0.598	5.479
TiO$_2$ + 2a + N719 + CDCA	37	11	12	0.635	5.654

The tested substrates with anchored dyes molecules showed thicknesses ranging from 8 to 12 µm. In the presented work, the thickness of the TiO$_2$ was measured using two methods, optical and SEM microscopes. The advantage of the SEM over the optical microscope is that the thickness of individual layers can be determined. However, that thickness determination using an optical microscope is a non-destructive method. The representative cross-sectional SEM image and micrograph of photoanodes are depicted in Figure 8 and Figure S14. On the SEM images the layer of glass, FTO and mesoporous TiO$_2$ were seen (cf. Figure 8 and Figure S14). Moreover, based on SEM, the presence of spherical TiO$_2$ nanoparticles was confirmed. Considering the data given in Table 2, it can be concluded that only small differences in the obtained thickness values of TiO$_2$ were observed using two independent measuring methods (SEM and optical microscope).

The values of surface quality parameters (RMS) determined by AFM were similar for most of the photoanodes tested. An increase in the roughness of the electrodes was observed when co-adsorbent was used. By analyzing the parameters S$_q$ and S$_{ku}$, it was possible to observe the trend of their change depending on the new dye used. In each of the three types of electrode structures, the mentioned parameters had lower values for compound **1a**. Moreover, similarly to the RMS values, the parameters described (S$_q$ and S$_{ku}$) increased after the addition of CDCA, which was due to lead to fewer dye molecules being anchored to the oxide substrate and thus less smoothing.
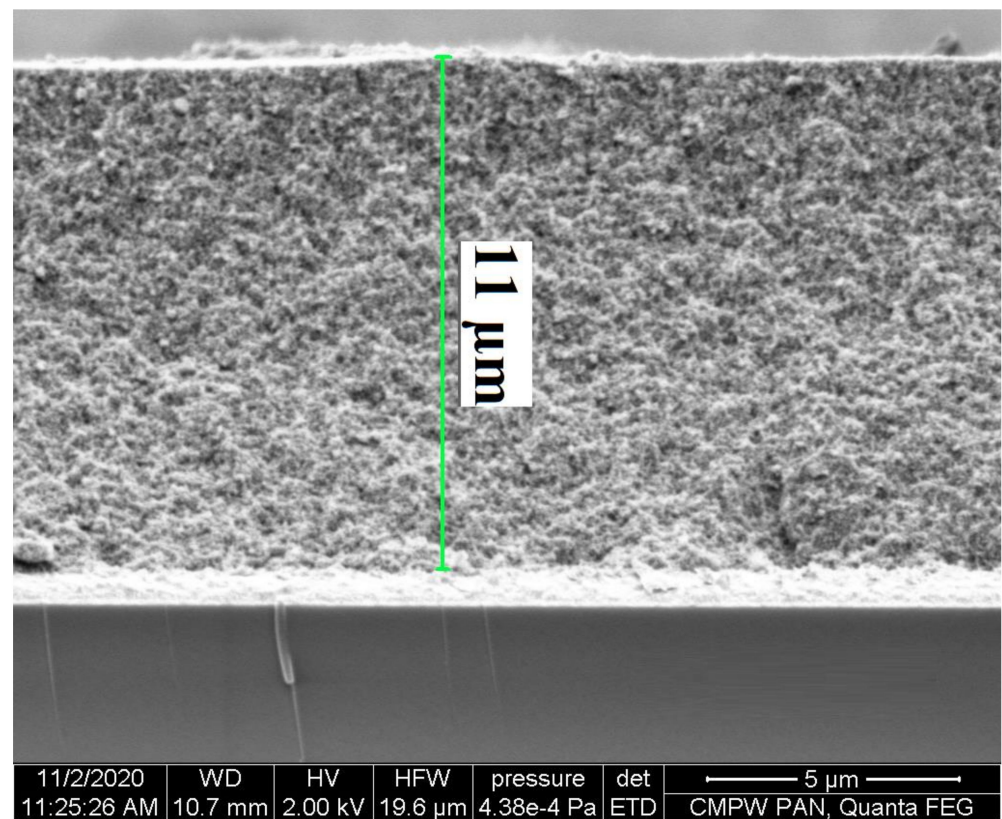
Figure 8. The cross-sectional SEM image of prepared TiO$_2$ substrate with anchored dyes mixture **2a** + N719 + CDCA.

3.3.2. Photovoltaic Properties of Devices

The photovoltaic (PV) properties of fabricated cells under standard AM 1.5 irradiations (100 mWcm^{-2}) were analyzed using current-voltage (J–V) characteristics and the electrochemical impedance spectroscopy (EIS). Based on J–V plots, open-circuit voltage (V$_{oc}$), photocurrent density (J$_{sc}$), fill factor (FF), and power conversion efficiency (PCE) were calculated as the PV parameters (cf. Table 3). Photocurrent density−voltage curves (J−V) of fabricated devices are presented in Figure 9.

Table 3. Photovoltaic parameters of fabricated dye-sensitized solar cells.

| Photoanode Sensitized with	V$_{oc}$ (V)	J$_{sc}$ (mA cm^{-2})	FF (–)	PCE (%)
N719	0.703 ($\pm$0.004)	14.28 ($\pm$0.03)	0.53 ($\pm$0.02)	5.35 ($\pm$0.04)
N719 + CDCA	0.762 ($\pm$0.003)	17.20 ($\pm$0.05)	0.50 ($\pm$0.01)	6.90 ($\pm$0.07)
1a	0.475 ($\pm$0.006)	0.30 ($\pm$0.03)	0.49 ($\pm$0.02)	0.07 ($\pm$0.01)
2a	0.567 ($\pm$0.002)	1.38 ($\pm$0.02)	0.57 ($\pm$0.01)	0.44 ($\pm$0.02)
1a + N719	0.680 ($\pm$0.002)	16.12 ($\pm$0.01)	0.51 ($\pm$0.01)	6.02 ($\pm$0.03)
2a + N719	0.670 ($\pm$0.002)	17.57 ($\pm$0.03)	0.53 ($\pm$0.01)	6.38 ($\pm$0.04)
1a + N719 + CDCA	0.700 ($\pm$0.003)	16.94 ($\pm$0.08)	0.53 ($\pm$0.01)	6.42 ($\pm$0.08)
2a + N719 + CDCA	0.716 ($\pm$0.001)	17.44 ($\pm$0.04)	0.57 ($\pm$0.01)	7.22 ($\pm$0.04)
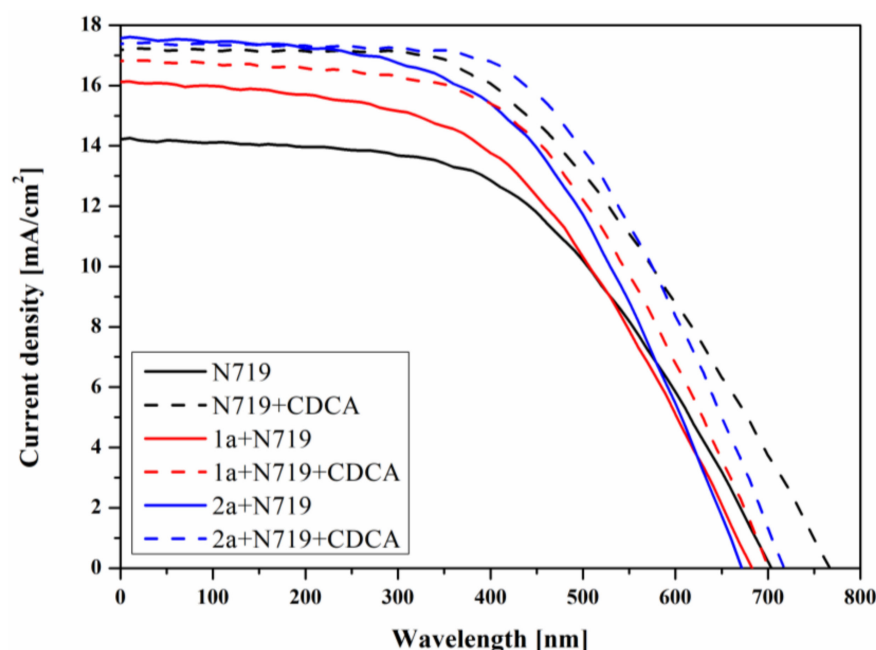
Figure 9. Photocurrent-voltage curves of prepared dye-sensitized solar cells.

As can be expected considering the UV-vis absorption range of synthesized **1a** and **2a**, the devices based on neat cyanoacrylic acids 10-hydroxobenzo[*h*]quinoline derivatives exhibited significantly lower PV performance compare to a reference cell based on N719. This is mainly due to low J_{sc} values, which are largely related to the absorption properties of the dyes. This was due to the relatively narrow range and lower absorbance of the studied compounds compare to N719 (cf. Figure S16). The utilization of the synthesized compounds as co-sensitizers allowed the increase of the PCE up to 6.02 and 6.38% (**1a** + N719 and **2a** + N719, respectively) compared to reference cell based on a neat N719 (PCE = 5.35%). The higher efficiency of the dye-mixed devices is mainly attributed to improvement in J_{sc}. The increase in J_{sc} was due to the extension of the absorption range of the photoanode containing a mixture of dyes, that is, N719 and cyanoacrylic acid 10-hydroxobenzo[*h*]quinoline derivatives compare to the absorption of the neat compounds (cf. Figure S16). The utilization of CDCA as co-adsorbent for photoanode preparation results in a further increase of PCE due to raising V_{oc}, J_{sc} and FF. In the case of CDCA addition, only the cell containing molecules **2a** and N719 showed a higher efficiency (7.22%) than the reference cell (6.90%). The cell prepared with dye **1a** and N719 had lower photovoltaic parameters, including efficiency (6.42%). In each case, devices containing the dye **2a** showed better efficiency than a solar cell with compound **1a** due to mainly higher reached short-circuit current density. Photoanodes containing anchored molecules of dye **1a** and N719, both with and without the addition of CDCA, had higher absorption compared to photoanodes based on **2a** and N719.

According to the DFT calculations concerning FMO energy levels, a device with 1a showed better performance than 2a. However, electrochemical impedance spectroscopy studies have shown differences in the layer-by-layer resistances of these two types of solar cells favoring cells containing compound **2a**.

To study the intrinsic charge transfer properties of the cells, the electrochemical impedance spectroscopy (EIS) technique was used. Impedance spectroscopy method involves analysis of investigated system response under AC conditions in a range of frequencies. Each cell under light exposure of simulated solar light source of 1000 Lm/m^2 was exposed to AC voltage signal. The DC voltage signal applied by a potentiostat was maintained at 0 V to reach short-circuit conditions. As each cell has its particular open-circuit voltage value, any particular non-zero voltage applied to different cells would result in electrodes' different polarization. Therefore, the short-circuit conditions were

chosen to measure impedance spectra as they allow us to compare the cells operating at the maximum current regime. The set of obtained impedance spectra are shown in Figure 10. Figure 10 gives a comparison between impedance spectra recorded in dark and under light illumination.
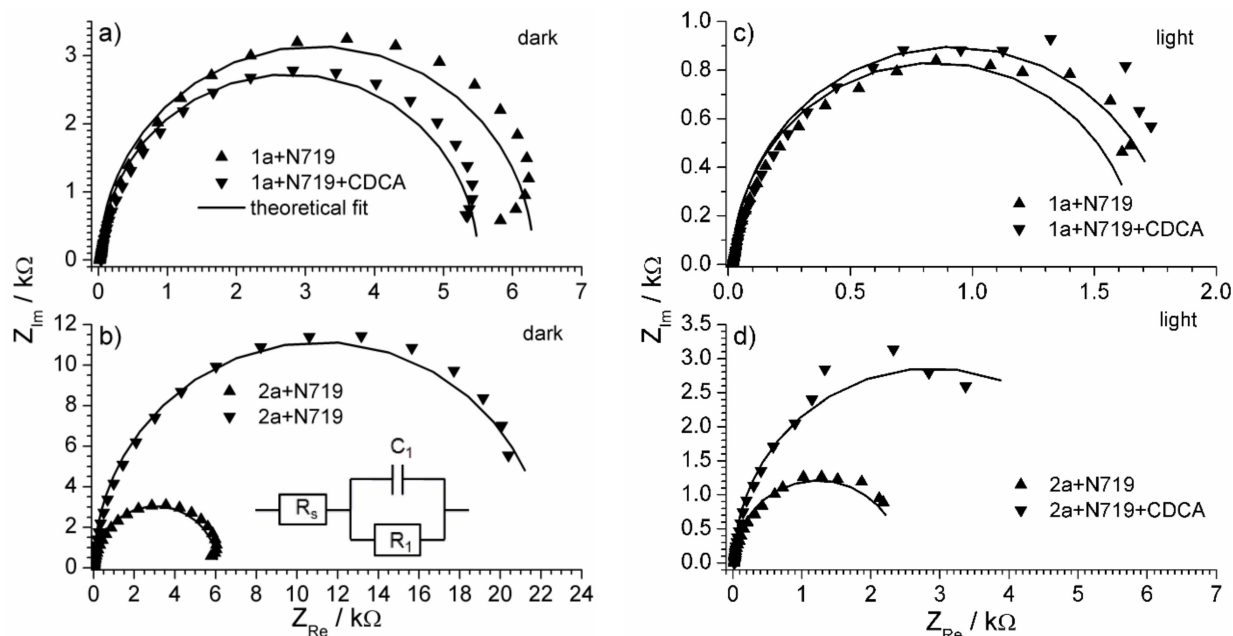

Figure 10. Impedance spectra (complex plane plots) of the studied cells: in darkness (**a**,**b**) and under light illumination (**c**,**d**). The photoanode dye component is shown in the legend. The equivalent electrical circuit is shown in the inset of part b.

The complex plane plots (Figure 10) have a semicircle, with minor deviations in the low-frequency region. The axis scales of the graph are deliberately made equal size to check the ideality of the semicircle, which is frequently observed and usually expected in the case of electrochemical systems.

The equivalent electrical circuit that fitted all the experimental spectra is shown in the inset of Figure 10. It describes the charge transport through the current-limiting electrode-solution interface. The cell includes two electrodes, and one could expect the appearance of two capacitance-resistance blocks in the model. However, in the case of a relatively high current, the limiting effect of one photoanode becomes crucial, thus the impedance of the counter electrode seems to be negligibly small to have an impact on total system impedance. Therefore, the effect of only a photosensitive semiconductor-solution interface could be revealed from impedance spectrum analysis.

Elements R_1 and C_1 correspond to a charge transport process that was limiting the DSSC operation within the low voltage range, with resistance R_1 being a charge transfer resistance of the cell. The physical sense of C_1 element is better described as a capacitance of the electrode-electrolyte interface. The calculated values of all four parameters for all five types of cells are shown in Table 4.

Table 4. Calculated values of the equivalent circuit parameters.

Compound	Dark			Light		
	R_s/Ω	$R_1/k\Omega$	$C_1/\mu F$	R_s/Ω	$R_1/k\Omega$	$C_1/\mu F$
N719 + CDCA	16.0	15.5	16.1	31.1	1.96	21.5
1a + N719	19.9	6.28	18.0	16.7	1.66	19.1
2a + N719	18.8	6.07	18.4	17.3	2.42	20.4
1a + N719 + CDCA	37.8	5.45	19.1	22.3	1.79	21.6
2a + N719 + CDCA	21.6	2.22	16.2	19.7	5.72	18.6

The resistance R_1 is considered the main parameter responsible for charge transfer rate through the electrode-solution interface. The values of its inverse value (charge transfer conductance) are compared in Figure 11.
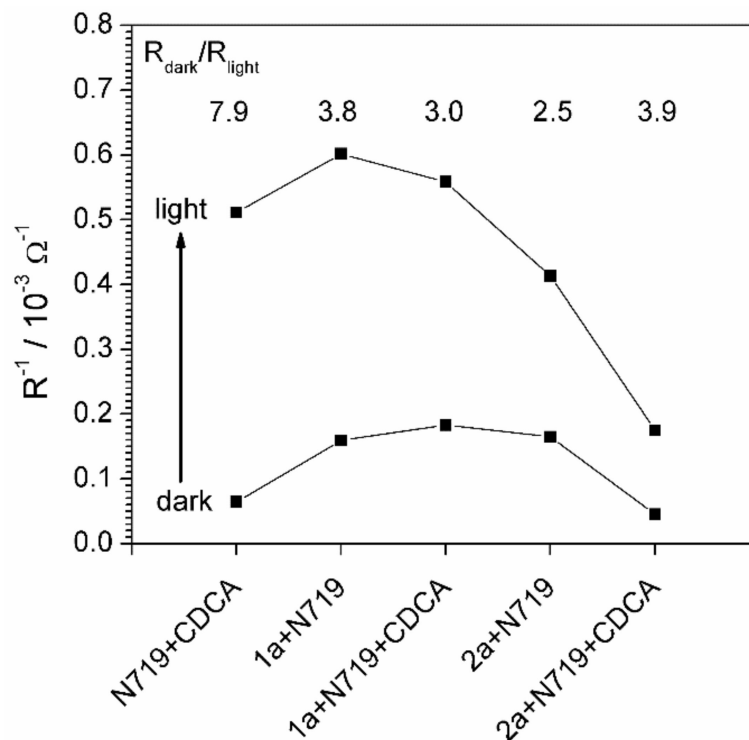

Figure 11. Inverse values of the charge transfer resistance compared for a set of cells in dark and under illumination. The calculated numerical increase of conductivity is given in the inscription.

The increase of R^{-1} value under illumination proves the photosensitivity of the electrode. The highest charge transfer conductivity (the lowest resistance) under light illumination was observed for the cell containing 1a active component (Figure 11). The charge transfer conductivity of the 2a based cells was smaller than the 1a based cells (Figure 11), however, the relative increase of conductivity under illumination was still high, especially in the case of 2a + N719 + CDCA sensitizer. The values of charge transfer resistance do not have to correspond directly to the photoconversion efficiency of the dye, which is a complex characteristic affected by many factors. The R value is not a photochemical, but an electrochemical parameter that describes the rate of charge transfer through the electrode-solution interface and is regarded to have the highest impact on the total internal resistance of the cell.

4. Conclusions

Two new benzo[*h*]quinolin-10-ol derivatives with one or two cyanoacrylic acid units were synthesized and characterized as well as tested as (co)-sensitizers DSSCs. Moreover, the beneficial impact of CDCA as a co-adsorbent was explained based on DFT calculations.

Summarizing the findings concerning the effect of the chemical structure of the prepared compounds, it was found that the introduction of a second anchoring group to benzo[*h*]quinolin-10-ol derivatives (i) significantly lowered melting temperature by about 65 °C but only slightly affected T_g, as well as its produced steel which is high at about 120 °C, (ii) lowered oxidation potential, and based on DFT in s **2a**@TiO_2 system, the dye orbitals have a certain share (14%) in the HOMO level. This is contrary to **1a**@TiO_2, where HOMO is located entirely on the dye (99%), and (iii) increased the molar absorption coefficient, slightly bathochromically shifted λ_{max}, and when adsorbed in TiO_2 showed a higher absorption range compared to **1a**@TiO_2.

The DFT calculations of the utilization effect of three co-adsorbents, CDCA, CA and CDA, revealed that due to the almost perpendicular adsorption of the CDCA molecule and a higher value of G_{ads}, CDCA seems to be a better co-adsorbent than others.

Considering the PV efficiency of fabricated solar cells based on synthesized molecules as co-sensitizers with N719, we improved the PCE value of about 12% (**1a**) and 19% (**2a**) with respect to the reference device based on a neat N719. The addition of CDCA increased the PCE of a reference cell from 5.35 to 6.90%. While the device with photoanode consists of a mixture of **2a**, N719 and CDCA showed a further increase of efficiency to 7.22%. Thus, the utilization of benzo[h]quinolin-10-ol derivative with two 2-cyanoacrylic acid units reduces the applied amount of N719 and enhances the DSSC performance.

Supplementary Materials: The following are available online at https://www.mdpi.com/article/10.3390/ma14123386/s1, The Supplementary Materials file included used materials, measurements, DSSC preparation description, DSC thermograms (Figure S1), absorption spectra and data (Figure S2, S3, and S16, and Table S1), fluorescence decays of tested dyes (Figure S4), electrochemical data (Figure S5, S6, and Table S2), DFT data of TiO_2 clusters, dyes (Tables S3–S6, Figures S7–S13), The cross-sectional SEM images of prepared TiO_2 (Figure S14) and optical microscope micrographs of electrodes (Figure S15).

Author Contributions: Conceptualization, E.S.-B.; investigation, A.S., G.S.-G., J.G.M., P.G., P.C., M.V., J.N., M.L., E.S.-B.; writing—original draft preparation, A.S., G.S.-G., J.G.M., P.G., P.C., M.V., E.S.-B.; writing—review and editing, A.S., J.G.M., J.N., E.S.-B. All authors have read the manuscript and agreed to the published.

Institutional Review Board Statement: Not applicable.

Informed Consent Statement: Not applicable.

Data Availability Statement: The data presented in this study are available on request from the corresponding author.

Conflicts of Interest: The authors declare no conflict of interest.

References

1. Grätzel, M. Recent advances in sensitized mesoscopic solar cells. *Acc. Chem. Res.* **2009**, *42*, 1788–1798. [CrossRef]
2. Shakeel Ahmad, M.; Pandey, A.K.; Abd Rahim, N. Advancements in the development of TiO_2 photoanodes and its fabrication methods for dye sensitized solar cell (DSSC) applications. A review. *Renew. Sustain. Energy Rev.* **2017**, *77*, 89–108. [CrossRef]
3. Breyer, C.; Bogdanov, D.; Aghahosseini, A.; Gulagi, A.; Child, M.; Oyewo, A.S.; Farfan, J.; Sadovskaia, K.; Vainikka, P. Solar photovoltaics demand for the global energy transition in the power sector. *Prog. Photovolt. Res. Appl.* **2018**, *26*, 505–523. [CrossRef]
4. Naik, P.; Elmorsy, M.R.; Su, R.; Babu, D.D.; El-Shafei, A.; Adhikari, A.V. New carbazole based metal-free organic dyes with D-π-A-π-A architecture for DSSCs: Synthesis, theoretical and cell performance studies. *Sol. Energy* **2017**, *153*, 600–610. [CrossRef]
5. O'Regan, B.; Grätzel, M. A low-cost, high-efficiency solar cell based on dye-sensitized colloidal TiO_2 films. *Nature* **1991**, *354*, 737–740. [CrossRef]
6. Lee, C.P.; Li, C.T.; Ho, K.C. Use of organic materials in dye-sensitized solar cells. *Mater. Today* **2017**, *20*, 267–283. [CrossRef]
7. Wu, Z.S.; Song, X.C.; Liu, Y.D.; Zhang, J.; Wang, H.S.; Chen, Z.J.; Liu, S.; Weng, Q.; An, Z.W.; Guo, W.J. New organic dyes with varied arylamine donors as effective co-sensitizers for ruthenium complex N719 in dye sensitized solar cells. *J. Power Sources* **2020**, *451*, 227776. [CrossRef]
8. Hagfeldt, A.; Boschloo, G.; Sun, L.; Kloo, L.; Pettersson, H. Dye-Sensitized Solar Cells. *Chem. Rev.* **2010**, *110*, 6595–6663. [CrossRef]
9. Johnson, N.M.; Smolin, Y.Y.; Hagaman, D.; Soroush, M.; Lau KK, S.; Ji, H.F. Suitability of N-propanoic acid spiropyrans and spirooxazines for use as sensitizing dyes in dye-sensitized solar cells. *Phys. Chem. Chem. Phys.* **2017**, *19*, 2981–2989. [CrossRef] [PubMed]
10. Sivanadanam, J.; Mukkamala, R.; Mandal, S.; Vedarajan, R.; Matsumi, N.; Aidhen, I.S.; Ramanujam, K. Exploring the role of the spacers and acceptors on the triphenylamine-based dyes for dye-sensitized solar cells. *Int. J. Hydrogen Energy* **2018**, *43*, 4691–4705. [CrossRef]

11. Ashraf, S.; Yildirim, E.; Akhtar, J.; Siddiqi, H.M.; El-Shafei, A. A comparative study of the influence of N,N′-dialkyl vs. N,N′-diaryl-based electron donor ancillary ligands on photocurrent and photovoltage in dye-sensitized solar cells (DSSCs). *Phys. Chem. Chem. Phys.* **2017**, *19*, 20847–20860. [CrossRef]

12. Desta, M.B.; Vinh, N.S.; Pavan Kumar, C.; Chaurasia, S.; Wu, W.T.; Lin, J.T.; Wei, T.C.; Diau, E. Pyrazine-incorporating panchromatic sensitizers for dye sensitized solar cells under one sun and dim light. *J. Mater. Chem. A* **2018**, *6*, 13778–13789. [CrossRef]

13. Elmorsy, M.R.; Abdel-Latif, E.; Badawy, S.A.; Fadda, A.A. Molecular geometry, synthesis and photovoltaic performance studies over 2-cyanoacetanilides as sensitizers and effective co-sensitizers for DSSCs loaded with HD-J. *Photochem. Photobiol. A Chem.* **2020**, *389*, 112239. [CrossRef]

14. Wang, G.; Wu, Y.; Ding, W.; Yu, G.; Hu, Z.; Wang, H.; Liu, S.; Zou, Y.; Pan, C. Photovoltaic performance of long-chain poly(triphenylamine-phenothiazine) dyes with a tunable π-bridge for dye-sensitized solar cells. *J. Mater. Chem. A* **2015**, *3*, 14217–14227. [CrossRef]

15. Su, R.; Elmorsy, M.R.; Abed, M.; Islam, A.; Lord, M.; Fadda, A.A.; El-Shafei, A. A Comparative Study on Two RuII Complexes with Thiophene-Based Ancillary Ligands for High-Efficiency Dye-Sensitized Solar Cells. *Eur. J. Inorg. Chem.* **2017**, *2017*, 3690–3697. [CrossRef]

16. Unny, D.; Kandregula, G.R.; Sivanadanam, J.; Ramanujam, K. Molecular engineering of pyrene carbazole dyes with a single bond and double bond as the mode of linkage. *N. J. Chem.* **2020**, *44*, 16511–16525. [CrossRef]

17. Carella, A.; Borbone, F.; Centore, R. Research progress on photosensitizers for DSSC. *Front. Chem.* **2018**, *6*, 1–24. [CrossRef]

18. Smestad, G.P. Education and solar conversion: Demonstrating electron transfer. *Sol. Energy Mater. Sol. Cells* **1998**, *55*, 157–178. [CrossRef]

19. Ye, M.; Wen, X.; Wang, M.; Iocozzia, J.; Zhang, N.; Lin, C.; Lin, Z. Recent advances in dye-sensitized solar cells: From photoanodes, sensitizers and electrolytes to counter electrodes. *Mater. Today* **2015**, *18*, 155–162. [CrossRef]

20. Cha, S.I.; Kim, Y.; Hwang, K.H.; Shin, Y.J.; Seo, S.H.; Lee, D.Y. Dye-sensitized solar cells on glass paper: TCO-free highly bendable dye-sensitized solar cells inspired by the traditional Korean door structure. *Energy Environ. Sci.* **2012**, *5*, 6071–6075. [CrossRef]

21. Zhang, L.; Cole, J.M. Anchoring groups for dye-sensitized solar cells. *ACS Appl. Mater. Interfaces* **2015**, *7*, 3427–3455. [CrossRef] [PubMed]

22. Błaszczyk, A. Strategies to improve the performance of metal-free dye-sensitized solar cells. *Dye Pigm.* **2018**, *149*, 707–718. [CrossRef]

23. Kula, S.; Szlapa-Kula, A.; Fabiańczyk, A.; Gnida, P.; Libera, M.; Bujak, K.; Siwy, M.; Schab-Balcerzak, E. Effect of thienyl units in cyanoacrylic acid derivatives toward dye-sensitized solar cells. *J. Photochem. Photobiol. B Biol.* **2019**, *197*, 111555. [CrossRef]

24. Wang, X.; Bolag, A.; Yun, W.; Du, Y.; Eerdun, C.; Zhang, X.; Bao, T.; Ning, J.; Alata, H.; Ojiyed, T. Enhanced performance of dye-sensitized solar cells based on a dual anchored diphenylpyranylidene dye and N719 co-sensitization. *J. Mol. Struct.* **2020**, *1206*, 127694. [CrossRef]

25. Fabiańczyk, A.; Gnida, P.; Chulkin, P.; Kula, S.; Filapek, M.; Szlapa-Kula, A.; Janeczek, H.; Schab-Balcerzak, E. Effect of heterocycle donor in 2-cyanoacrylic acid conjugated derivatives for DSSC applications. *Sol. Energy* **2020**, *220*, 1109–1119. [CrossRef]

26. Luo, J.; Wan, Z.; Jia, C.; Wang, Y.; Wu, X.; Yao, X. Co-sensitization of Dithiafulvenyl-Phenothiazine Based Organic Dyes with N719 for Efficient Dye-Sensitized Solar Cells. *Electrochim. Acta* **2016**, *211*, 364–374. [CrossRef]

27. Kotowicz, S.; Sęk, D.; Kula, S.; Fabiańczyk, A.; Małecki, J.G.; Gnida, P.; Maćkowski, S.; Siwy, M.; Schab-Balcerzak, E. Photoelectrochemical and thermal characterization of aromatic hydrocarbons substituted with a dicyanovinyl unit. *Dyes Pigm.* **2020**, *180*, 108432. [CrossRef]

28. Lee, K.M.; Hsu, Y.C.; Ikegami, M.; Miyasaka, T.; Justin Thomas, K.R.; Lin, J.T.; Ho, K.C. Co-sensitization promoted light harvesting for plastic dye-sensitized solar cells. *J. Power Sources* **2011**, *196*, 2416–2421. [CrossRef]

29. Singh, S.P.; Chandrasekharam, M.; Gupta, K.S.V.; Islam, A.; Han, L.; Sharma, G.D. Co-sensitization of amphiphilic ruthenium (II) sensitizer with a metal free organic dye: Improved photovoltaic performance of dye sensitized solar cells. *Org. Electron.* **2013**, *14*, 1237–1241. [CrossRef]

30. Su, R.; Lyu, L.; Elmorsy, M.R.; El-Shafei, A. Structural studies and photovoltaic investigation of indolo[2,3-b] quinoxaline-based sensitizers/co-sensitizers achieving highly efficient DSSCs. *N. J. Chem.* **2020**, *44*, 2797–2812. [CrossRef]

31. Keremane, K.; Abdellah, I.M.; Naik, P.; El-Shafei, A.; Adhikari, A.V. Simple thiophene-bridged D–π–A type chromophores for DSSCs: Comprehensive study of their sensitization and co-sensitization properties. *Phys. Chem. Chem. Phys.* **2020**, *22*, 23169–23184. [CrossRef] [PubMed]

32. Elmorsy, M.R.; Su, R.; Abdel-Latif, E.; Badawy, S.A.; El-Shafei, A.; Fadda, A.A. New cyanoacetanilides based dyes as effective co-sensitizers for DSSCs sensitized with ruthenium (II) complex (HD-2). *J. Mater. Sci. Mater. Electron.* **2020**, *31*, 7981–7990. [CrossRef]

33. Tanaka, E.; Michaels, H.; Freitag, M.; Robertson, N. Synergy of co-sensitizers in a copper bipyridyl redox system for efficient and cost-effective dye-sensitized solar cells in solar and ambient light. *J. Mater. Chem. A* **2020**, *8*, 1279–1287. [CrossRef]

34. Elmorsy, M.R.; Lyu, L.; Su, R.; Abdel-Latif, E.; Badawy, S.A.; El-Shafei, A.; Fadda, A.A. Co-sensitization of the HD-2 complex with low-cost cyanoacetanilides for highly efficient DSSCs. *Photochem. Photobiol. Sci.* **2020**, *19*, 281–288. [CrossRef] [PubMed]

35. Cole, J.M.; Pepe, G.; Al Bahri, O.K.; Cooper, C.B. Cosensitization in Dye-Sensitized Solar Cells. *Chem. Rev.* **2019**, *119*, 7279–7327. [CrossRef]

36. Lee, H.; Kim, J.; Kim, D.Y.; Seo, Y. Co-sensitization of metal free organic dyes in flexible dye sensitized solar cells. *Org. Electron.* **2018**, *52*, 103–109. [CrossRef]

37. Islam, A.; Akhtaruzzaman, M.; Chowdhury, T.H.; Qin, C.; Han, L.; Bedja, I.M.; Stalder, R.; Schanze, K.S.; Reynolds, J.R. Enhanced Photovoltaic Performances of Dye-Sensitized Solar Cells by Co-Sensitization of Benzothiadiazole and Squaraine-Based Dyes. *ACS Appl. Mater. Interfaces* **2016**, *8*, 4616–4623. [CrossRef]

38. Hao, Y.; Saygili, Y.; Cong, J.; Eriksson, A.; Yang, W.; Zhang, J.; Polanski, E.; Nonomura, K.; Zakeeruddin, S.M.; Grazel, M.; et al. Novel Blue Organic Dye for Dye-Sensitized Solar Cells Achieving High Efficiency in Cobalt-Based Electrolytes and by Co-Sensitization. *ACS Appl. Mater. Interfaces* **2016**, *8*, 32797–32804. [CrossRef]

39. Chen, Y.; Zeng, Z.; Li, C.; Wang, W.; Wang, X.; Zhang, B. Highly efficient co-sensitization of nanocrystalline TiO$_2$ electrodes with plural organic dyes. *N. J. Chem.* **2005**, *29*, 773–776. [CrossRef]

40. Clifford, J.N.; Forneli, A.; Chen, H.; Torres, T.; Tan, S.; Palomares, E. Co-sensitized DSCs: Dye selection criteria for optimized device Vocand efficiency. *J. Mater. Chem.* **2011**, *21*, 1693–1696. [CrossRef]

41. Lin, L.Y.; Yeh, M.H.; Lee, C.P.; Chang, J.; Baheti, A.; Vittal, R.; Thomas, K.R.; Ho, K.C. Insights into the co-sensitizer adsorption kinetics for complementary organic dye-sensitized solar cells. *J. Power. Sources* **2014**, *247*, 906–914. [CrossRef]

42. Wantulok, J.; Szala, M.; Quinto, A.; Nycz, J.E.; Giannarelli, S.; Sokolova, R.; Książek, M.; Kusz, J. Synthesis and electrochemical and spectroscopic characterization of selected quinolinecarbaldehydes and Schiff bases as their derivatives. *Molecules* **2020**, *25*, 2053. [CrossRef] [PubMed]

43. Frisch, M.J.; Trucks, G.W.; Schlegel, H.B.; Scuseria, G.E.; Robb, M.A.; Cheeseman, J.R.; Scalmani, G.; Barone, V.; Petersson, G.A.; Nakatsuji, H.; et al. *Gaussian 16, Revision C.01*; Gaussian, Inc.: Wallingford, CT, USA, 2019.

44. Becke, A.D. Density-functional exchange-energy approximation with correct asymptotic-behavior. *Phys. Rev. A* **1988**, *38*, 3098. [CrossRef] [PubMed]

45. Perdew, J.P. Density-functional approximation for the correlation energy of the inhomogeneous electron gas. *Phys. Rev. B* **1986**, *33*, 8822. [CrossRef] [PubMed]

46. Ditchfield, R.; Hehre, W.J.; Pople, J.A. Self-consistent molecular-orbital methods. IX. An extended gaussian-type basis for molecular-orbital studies of organic molecules. *J. Chem. Phys.* **1971**, *54*, 724–728. [CrossRef]

47. Lee, C.; Yang, W.; Parr, R.G. Development of the Colle-Salvetti correlation-energy formula into a functional of the electron density. *Phys. Rev. B* **1988**, *37*, 785–789. [CrossRef] [PubMed]

48. O'Boyle, N.M.; Tenderholt, A.L.; Langner, K.M. Software News and Updates cclib: A Library for Package-Independent Computational Chemistry Algorithms. *J. Comp. Chem.* **2008**, *29*, 839–845. [CrossRef]

49. Mas-Montoya, M.; Janssen, R.A.J. The Effect of H- and J-Aggregation on the Photophysical and Photovoltaic Properties of Small Thiophene–Pyridine–DPP Molecules for Bulk-Heterojunction Solar Cells. *Adv. Funct. Mater.* **2017**, *27*, 1605779. [CrossRef]

50. Thogiti, S.; Vuppala, S.; Cha, H.L.; Thuong, N.T.; Jo, H.J.; Chitumalla, R.K.; Hee, S.C.; Thuy, C.T.; Jang, J.; Jung, J.H.; et al. Enhanced DSSC performance by the introduction of hydroxamic acid group into the cyanoacetic acid dyes. *J. Photochem. Photobiol. A* **2020**, *398*, 112512. [CrossRef]

51. Gnida, P.; Libera, M.; Pająk, A.; Schab-Balcerzak, E. Examination of the Effect of Selected Factors on the Photovoltaic Response of Dye-Sensitized Solar Cells. *Energy Fuels* **2020**, *34*, 14344–14355. [CrossRef]

52. Wan, W.; Wang, H.; Lin, H.; Wang, J.; Jiang, Y.; Jiang, H.; Zhu, S.; Wang, Z.; Hao, J. Synthesis, electrochemical, photophysical, and electroluminescent properties of organic dyes containing pyrazolo[3, 4-b]quinoline chromophore. *Dyes Pigm.* **2015**, *121*, 138–146. [CrossRef]

53. Slodek, A.; Zych, D.; Maroń, A.; Gawecki, R.; Mrozek-Wilczkiewicz, A.; Malarz, K.; Musiol, R. Phenothiazine derivatives—Synthesis, characterization, and theoretical studies with an emphasis on the solvatochromic properties. *J. Mol. Liq.* **2019**, *285*, 515–525. [CrossRef]

54. Cidlina, A.; Novakova, V.; Miletin, M.; Zimcik, P. Peripheral substitution as a tool for tuning electron-accepting properties of phthalocyanine analogs in intramolecular charge transfer. *Dalt. Trans.* **2015**, *44*, 6961–6971. [CrossRef]

55. Slodek, A.; Zych, D.; Golba, S.; Zimosz, S.; Gnida, P.; Schab-Balcerzak, E. Dyes based on the D/A-acetylene linker-phenothiazine system for developing efficient dye-sensitized solar cells. *J. Mater. Chem. C* **2019**, *7*, 5830–5840. [CrossRef]

56. Zhang, J.; Yu, C.; Wang, L.; Li, Y.; Ren, Y.; Shum, K. Energy barrier at the N719-dye/CsSnI$_3$ interface for photogenerated holes in dye-sensitized solar cells. *Sci. Rep.* **2014**, *4*, 3–8. [CrossRef]

57. De Angelis, F.; Fantacci, S.; Mosconi, E.; Nazeeruddin, M.K.; Grätzel, M. Absorption spectra and excited state energy levels of the N719 dye on TiO2 in dye-sensitized solar cell models. *J. Phys. Chem. C* **2011**, *115*, 8825–8831. [CrossRef]

58. Argazzi, R.; Bignozzi, C.A.; Heimer, T.A.; Castellano, F.N.; Meyer, G.J. Enhanced Spectral Sensitivity from Ruthenium(II) Polypyridyl Based Photovoltaic Devices. *Inorg. Chem.* **1994**, *33*, 5741–5749. [CrossRef]

59. Chung, I.; Lee, B.; He, J.; Chang RP, H.; Kanatzidis, M.G. All-solid-state dye-sensitized solar cells with high efficiency. *Nature* **2012**, *485*, 486–489. [CrossRef]

60. Fattori, A.; Peter, L.M.; Belding, S.R.; Compton, R.G.; Marken, F. Cis-bis(isothiocyanato)-bis(2,2'-bipyridyl-4,4'dicarboxylato)-Ru(II) (N719) dark-reactivity when bound to fluorine-doped tin oxide (FTO) or titanium dioxide (TiO$_2$) surfaces. *J. Electroanal. Chem.* **2010**, *640*, 61–67. [CrossRef]

61. Hou, R.; Yuan, S.; Ren, X.; Zhao, Y.; Wang, Z.; Zhang, M.; Li, D.; Shi, L. Effects of acetyl acetone-typed co-adsorbents on the interface charge recombination in dye-sensitized solar cell photoanodes. *Electrochim. Acta* **2015**, *154*, 190–196.

62. Saranya, G.; Yam, C.; Gao, S.; Chen, M. Roles of Chenodeoxycholic Acid Coadsorbent in Anthracene-Based Dye-Sensitized Solar Cells: A Density Functional Theory Study. *J. Phys. Chem. C* **2018**, *122*, 23280–23287. [CrossRef]
63. Becke, A.D. Density-functional thermochemistry. III. The role of exact exchange. *J. Chem. Phys.* **1993**, *98*, 5648–5652. [CrossRef]
64. Becke, A.D. Density-functional thermochemistry. IV. A new dynamical correlation functional and implications for exact-exchange mixing. *J. Chem. Phys.* **1996**, *104*, 1040–1046. [CrossRef]
65. Hsu, C.P.; Lee, K.M.; Huang JT, W.; Lin, C.Y.; Lee, C.H.; Wang, L.P.; Tsai, S.Y.; Ho, K.C. EIS analysis on low temperature fabrication of TiO_2 porous films for dye-sensitized solar cells. *Electrochim. Acta* **2008**, *53*, 7514–7522. [CrossRef]
66. Kao, M.C.; Chen, H.Z.; Young, S.L.; Kung, C.Y.; Lin, C.C. The effects of the thickness of TiO_2 films on the performance of dye-sensitized solar cells. *Thin Solid Films* **2009**, *517*, 5096–5099. [CrossRef]